Universality of internal structure characteristics in granular media under shear

Shiwei Zhao [*] and Jidong Zhao [†]
Department of Civil and Environmental Engineering, The Hong Kong University of Science and Technology, Clearwater Bay, Kowloon, Hong Kong

Ning Guo [‡]
College of Civil Engineering and Architecture, Zhejiang University, Hangzhou 310058, China

(Received 23 September 2019; published 22 January 2020)

We examine the signatures of internal structure emerged from quasistatic shear responses of granular materials based on three-dimensional discrete element simulations. Granular assemblies consisting of spheres or nonspherical particles of different polydispersity are sheared from different initial densities and under different loading conditions (drained or undrained) steadily to reach the critical state (a state featured by constant stress and constant volume). The radial distribution function used to measure the packing structure is found to remain almost unchanged during the shearing process, regardless of the initial states or loading conditions of an assembly. Its specific form, however, varies with polydispersities in both grain size and grain shape. Set Voronoi tessellation is employed to examine the characteristics of local volume and anisotropy, and deformation. The local inverse solid fraction and anisotropy index are found following inverse Weibull and log-normal distributions, respectively, which are unique at the critical states. With further normalization, an invariant distribution for local volume and anisotropy is observed whose function can be determined by the polydispersities in both particle size and grain shape but bears no relevance to initial densities or loading conditions (or paths). An invariant Gaussian distribution is found for the local deformation for spherical packings, but no invariant distribution can be found for nonspherical packings where the distribution of normalized local volumetric strain is dependent on initial states.

DOI: 10.1103/PhysRevE.101.012906

I. INTRODUCTION

Granular materials are typical complex systems featuring large numbers of discrete particles interacting nonlinearly through contacts and rolling and forming strongly heterogeneous and amorphous internal structures. The characteristics of internal structure (also called fabric) are widely considered, bearing close correlations with the physical properties and mechanical behaviors of a granular material [1–3]. However, it remains challenging to identify the key features of internal structure to directly relate them to the macroscopic properties to render rigorous cross-scale understandings. To demystify the complexity of granular systems, statistical mechanics theories have been developed, exemplified by those proposed by Edwards and coauthors [4,5], highlighting the role of volume (or density) in describing the jammed behavior of static granular media. The local properties, especially the local volume fluctuation, have been a focus of interest in numerous experimental and numerical studies [6–11]. For example, Aste and coauthors [7,8] revealed an invariant distribution in local volume for static monodisperse sphere packings. This universality was further confirmed for monodisperse ellipsoid packings [12]. However, its validity remains to be verified for general granular materials with polydispersity in both particle size and shape, i.e., for polydisperse and poly-shaped nonspherical particles, which are widely encountered in nature, industry, and engineering.

The majority of existing studies on local properties have been focused on certain specific states such as the stationary state [8], the jamming transition state [13], or the sheared steady state [14]. Evidently, particles will experience steady rearrangement when subjected to shear, resulting in constantly evolving local structures and unrecoverable (plastic) deformation, often incurring strain localization. Investigating the evolution of local structure and deformation during a typical shearing process may shed new light on the local properties of sheared granular materials. Indeed, based on discrete element simulations, Guo and Zhao [11] found some invariant distributions in local properties such as local volume and local anisotropy during constant-volume shearing of dense sphere assemblies. Despite the fact that the mechanical responses of sheared granular materials have been extensively explored in the past (see Refs. [2,15–19]), there are relatively scarce studies on the fluctuations of local properties of sheared granular materials in the literature, especially for nonspherical assemblies.

This study aims to rigorously examine the significance of polydispersity in both particle size and shape on the mechanical behaviors of granular materials [18,20–23]. Using the

[*] ceswzhao@ust.hk
[†] jzhao@ust.hk
[‡] nguo@zju.edu.cn

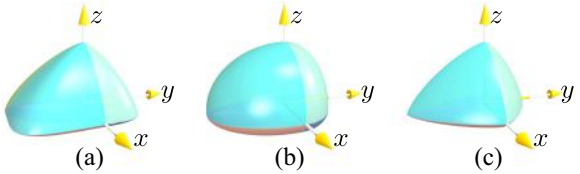

FIG. 1. Poly-superellipsoids with $r_x^+ = 1.0$, $r_x^- = 0.5$, $r_y^+ = 0.8$, $r_y^- = 0.9$, $r_z^+ = 0.4$, $r_z^- = 0.6$ and (a) $\epsilon_1 = 0.4$, $\epsilon_2 = 1.5$, (b) $\epsilon_1 = \epsilon_2 = 1.0$, (c) $\epsilon_1 = \epsilon_2 = 1.5$.

discrete element method (DEM), we analyze and compare the shear responses of specimens composed of monodisperse and polydisperse spheres and nonspheres, with different initial states and under different loading conditions. The loading conditions include both constant confining pressure and constant-volume (or drained and undrained, in soil mechanics) triaxial shear. The characteristics of local structure and deformation are examined, with special attention on the differences observed in sphere and nonsphere assemblies. In particular, we wish to explore whether there is a universality in local structure and deformation of sheared granular materials if the effects of polydispersity in particle size and shape, initial states, and loading conditions are all taken into account.

This paper is organized as follows. The details of numerical approach and model setup are introduced first in Sec. II, followed by analysis of the mechanical responses at the macroscopic scale in Sec. III. The main focus is placed in Sec. IV on the analysis of the granular microstructure to identify the characteristics of local structure and deformation. Major findings of this work are summarized in Sec. V.

II. NUMERICAL PROCEDURES

A. Particle shape

In this study, we model nonspherical particle shape using a poly-superellipsoid-based approach recently proposed [24]. It has been proved to be versatile and efficient in capturing the major shape features (such as elongation, flatness, asymmetry, and angularity) of realistic particles in nature, such as sand. In this method, a poly-superellipsoid particle is constructed by assembling eight pieces of superellipsoids according to the following surface function defined in a local Cartesian coordinate system:

$$\left(\left|\frac{x}{r_x}\right|^{\frac{2}{\epsilon_1}} + \left|\frac{y}{r_y}\right|^{\frac{2}{\epsilon_1}}\right)^{\frac{\epsilon_1}{\epsilon_2}} + \left|\frac{z}{r_z}\right|^{\frac{2}{\epsilon_2}} = 1, \tag{1}$$

with

$$r_x = r_x^+ \quad \text{if} \quad x \geqslant 0 \quad \text{else} \quad r_x^-, \tag{2a}$$
$$r_y = r_y^+ \quad \text{if} \quad y \geqslant 0 \quad \text{else} \quad r_y^-, \tag{2b}$$
$$r_z = r_z^+ \quad \text{if} \quad z \geqslant 0 \quad \text{else} \quad r_z^-, \tag{2c}$$

where r_x^+, r_y^+, r_z^+ and r_x^-, r_y^-, r_z^- are the principal elongation along the positive and negative directions of x, y, z axes, respectively; ϵ_1, ϵ_2 control the squareness or blockiness of the particle surface; and their possible values are within (0,2) for convex shapes. Figure 1 demonstrates how ϵ_1 and ϵ_2 control the generated particle surface. To quantify particle shape, two auxiliary descriptors, namely, principal length l_x, l_y, l_z and principal eccentricity e_x, e_y, e_z, are introduced such that

$$r_x^+ = l_x e_x, \quad r_x^- = l_x(1 - e_x), \tag{3a}$$
$$r_y^+ = l_y e_y, \quad r_y^- = l_y(1 - e_y), \tag{3b}$$
$$r_z^+ = l_z e_z, \quad r_z^- = l_z(1 - e_z). \tag{3c}$$

B. Simulation setup and packing preparation

The simulations are carried out by means of the discrete element method with an open-source DEM platform Sudo-DEM [19,24,25], developed by the authors. The basic particle element is the poly-superellipsoid, as introduced in Sec. II A, based on which a rich library of particle shapes with moderate increase in computational complexity (e.g., in contact detection) as compared with sphere elements can be generated. For the sake of computational efficiency, a linear spring contact model [11] in conjunction with a Coulomb sliding model is employed according to the following expressions to compute the normal and tangential contact forces $\boldsymbol{f}_n^c$ and $\boldsymbol{f}_t^c$ at a given contact c:

$$\boldsymbol{f}_n^c = -k_n \delta \boldsymbol{n}^c, \tag{4a}$$
$$\boldsymbol{f}_t^c = -\min\left\{\mu\left|\boldsymbol{f}_n^c\right|, \left|\boldsymbol{f}_t^{c'} - k_t \boldsymbol{u}^c\right|\right\}\boldsymbol{u}^c/|\boldsymbol{u}^c|, \tag{4b}$$

where k_n and k_t are normal and tangential contact stiffness, respectively; δ is the overlap between two particles calculated by using the common normal method (referring to our previous work [24] for details), which should be sufficiently small (smaller than 10^{-2} particle size in this work) to reduce its side effect on the configuration of a granular system [26]; μ is the coefficient of sliding friction; $\boldsymbol{n}^c$ is the outward contact normal; $\boldsymbol{f}_t^{c'}$ is the tangential contact force at the last time step but rotated into the current contact plane; and $\boldsymbol{u}^c$ is the tangential displacement during the current time step. Note that particle size is defined as the radius of an equivalent sphere with the same volume as the nonspherical particle. As for the material property, the friction coefficient μ is set to 0.3 (a typical value for quartz sands), while the contact stiffness is empirically set as $k_n = k_s = r \times 100$ MPa (where r is the average particle size) to yield reasonable Young's modulus and Poisson's ratio for quartz sands [17,19]. Although the contact stiffness affects the mechanical behaviors of a granular material [27], the magnitudes of k_n and k_s adopted here ensure comparable results with using the Hertz-Mindlin model as reported in the literature [19].

Three groups of numerical specimens for nonspheres and spheres are prepared with the following protocol: (a) There are 10 000 particles with random orientations and positions generated within a cubic container, where particle shape parameters are uniformly selected from the intervals given in Table I. Note that the selected range of particle blockiness covers a broad diversity of the particle shape due to the fact that the particle surface varies in an exponential-like decay manner with ϵ_1 and ϵ_2 away from 1.0. With the given ranges of shape parameters, the most distorted shape has a maximum aspect ratio of 3.0 and a maximum eccentricity of 4.0, which is an extreme case for realistic sandy grains in nature. (b) Isotropic compression is performed on each initial assembly, and all confining plates maintain a constant confining stress σ_0

TABLE I. Three groups of particle shape parameters.

Group[a]	ϵ_1, ϵ_2	l_x, l_y, l_z (mm)	e_x, e_y, e_z
NS	[0.5,1.4]	[0.25,0.75]	[0.2, 0.8]
PS	[1.0,1.0]	[0.25,0.75]	[0.5,0.5]
MS	[1.0,1.0]	[0.50,0.50]	[0.5,0.5]

[a]NS: polydisperse nonspheres; PS: polydisperse spheres; MS: monodisperse spheres.

of 100 kPa via the so-called stress-controlled numerical servo mechanism. (c) The isotropic compression terminates with $\alpha_f \leqslant 0.01, \beta_f \leqslant 0.01, \gamma_f \leqslant 0.001$, where α_f is the mean stress ratio, β_f the deviatoric stress ratio, and γ_f unbalanced force ratio, respectively given by

$$\alpha_f = \frac{|p-\sigma_0|}{\sigma_0}, \beta_f = \frac{q}{p}, \gamma_f = \frac{\sum_{B_j \in V} \left|\sum_{c\in B_j} \boldsymbol{f}_j^c + \boldsymbol{f}_j^b\right|}{2\sum_{c\in V}|\boldsymbol{f}^c|}, \tag{5}$$

in which p and q denote the mean stress and deviatoric stress, respectively, given later in Eqs. (7a) and (7b), $\boldsymbol{f}_j^c$ and $\boldsymbol{f}_j^b$ are total contact force and body force of the jth particle, and $\boldsymbol{f}^c$ is contact force at contact c.

Each group consists of three packings with different initial densities. A total of nine packings are prepared with corresponding characteristics summarized in Table II, where e_0 is the initial void ratio (i.e., ratio of void volume to solid volume within a packing) of a packing before shear, and $\langle Z\rangle$ is the mean coordination number (average number of contacts per particle). Snapshots of two initial specimens with nonspherical and spherical particles, NS-D and PS-D, are exemplified in Fig. 2.

C. Numerical shear

The specimens are sheared under triaxial compression conditions, where the top and bottom plates push the specimen from both sides at a constant axial strain rate $\dot{\epsilon}_z$ to trigger a continuous shear process. All specimens are subjected to two typical loading conditions commonly encountered in soil mechanics: drained and undrained. For drained loading, the four side plates exert a constant confining stress σ_0 onto the specimen when the top and the bottom plates move; for the undrained case, a specimen is so sheared to maintain a constant volume by adjusting the positions of the four side plates according to $\dot{\epsilon}_x = \dot{\epsilon}_y = -\dot{\epsilon}_z/2$. It is worth noting that particles in the simulations are dry and the constant-volume condition is used as a mere approximation as the real undrained condition in the laboratory [17,28]. To ensure quasistatic shear, the axial strain rate $\dot{\epsilon}_z$ is set to a small value of 0.01/s, fulfilling the criterion that the inertia number $I = \dot{\epsilon}_z\langle d\rangle\sqrt{\bar{\rho}/\sigma_0} \leqslant 10^{-3}$ [15,16], where $\langle d\rangle$ is the average particle diameter and $\bar{\rho}$ is the material mass density (2650 kg/m^3 for quartz sands). Note that the mass density is scaled up by 6 orders of magnitude for achieving a large time step, i.e., 5×10^{-5} s in DEM simulations. More details on the numerical shear can be found in [19]. Specimens subjected to the undrained loading, except for the loose ones, are compressed to a sufficiently large level of axial strain $\epsilon_z = 50\%$, at which

TABLE II. Characteristics of initial specimens for nonspheres and spheres.

Group	Label[a]	e_0	$\langle Z\rangle$	Description
NS	NS-D	0.429	8.897	Dense
	NS-M	0.554	5.907	Medium dense
	NS-L	0.641	5.489	Loose
PS	PS-D	0.564	5.509	Dense
	PS-M	0.594	5.391	Medium dense
	PS-L	0.725	3.965	Loose
MS	MS-D	0.622	6.171	Dense
	MS-M	0.708	5.244	Medium dense
	MS-L	0.766	4.773	Loose

[a]A-B: A for group tag; B for dense (D), medium dense (M) or loose (L).

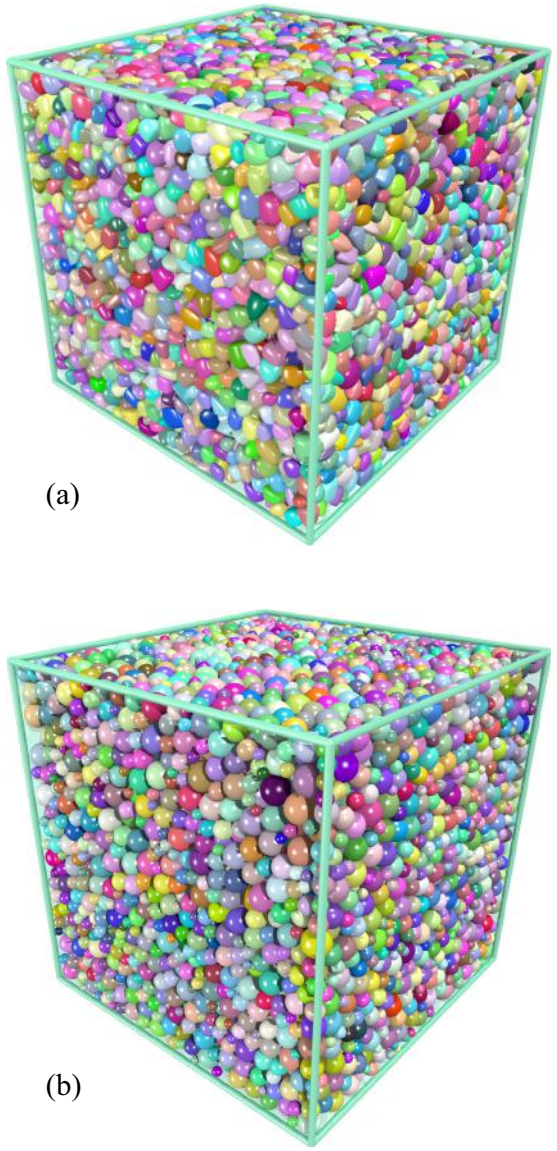

FIG. 2. Snapshots of initial assemblies (a) NS-D and (b) S-D composed of 10 000 nonspherical and spherical particles, respectively.

the specimens reach the steady flow regime (or critical state in soil mechanics). We label the different specimens under variable loading conditions according to the following A-B-C grouping to facilitate discussion: A stands for the group tag (NS for polydisperse nonspheres, PS for polydisperse spheres, and MS for monodisperse spheres); B denotes either drained (D) or undrained (U) loading conditions; and C stands for the initial state, either dense (D), medium dense (M), or loose (L).

III. MECHANICAL BEHAVIOR AT THE MACROSCALE

The following stress tensor defined by [29] based on volume average contact forces of an assembly is adopted to represent the macroscopic mechanical response of a specimen during shearing:

$$\boldsymbol{\sigma} = \frac{1}{V}\sum_{c\in V} \boldsymbol{f}^c \otimes \boldsymbol{l}^c, \tag{6}$$

where V is the total volume of the assembly, $\boldsymbol{f}^c$ is the contact force at contact c, $\boldsymbol{l}^c$ is the branch vector joining the centers of the two contacting particles at contact c, and $\otimes$ denotes the dyadic product. Two commonly used invariants of $\boldsymbol{\sigma}$, the mean stress p and the deviatoric stress q, are defined as

$$p = \frac{1}{3}\mathrm{tr}\,\boldsymbol{\sigma}, \tag{7a}$$

$$q = \sqrt{\frac{3}{2}\mathrm{dev}\,\boldsymbol{\sigma} : \mathrm{dev}\,\boldsymbol{\sigma}}. \tag{7b}$$

The deformation of a specimen is quantified by the axial strain ϵ_z and the volumetric strain ϵ_v, which can be approximately calculated from the positions of the boundary walls, i.e., $\epsilon_z = \ln(H_0/H)$, $\epsilon_v = \ln(V_0/V)$, where H and V are the height and volume of the specimen during shearing, respectively, and H_0 and V_0 are their initial values before shear. Negative values of volumetric strain indicate dilation.

Figure 3 shows the stress paths for the three groups of specimens under the two drainage conditions. Notably, the stress paths for the drained cases (e.g., NS-D-D, NS-D-M, and NS-D-L in NS) are approximately straight lines with a slope of 3 : 1, which is consistent with the theoretical slope ($dq/dp = 3$), typically for a conventional triaxial compression test in soil mechanics. As for the undrained cases, the loading path is strongly affected by the initial state of a specimen. While a dense specimen shows a general nonlinear increase of the deviatoric stress q with the mean stress p before reaching a critical state line (CSL), a medium dense specimen may experience an initial drop in p before p and q reach the so-called phase transformation point and both increase with shear again. For a loose specimen, p shows a steady decrease during shearing (i.e., losing effective confining stress), accompanied by an initial increase in q followed by a steady drop, until both p and q become zero (see, e.g., NS-U-L, PS-U-L, and MS-U-L). The specimen reaches the so-called liquefaction state and can no longer undertake any external loading. The quasistatic shear-induced liquefaction under constant volume suggests that a jamming transition may be triggered by shear even at a constant global solid fraction. The underlying mechanism can

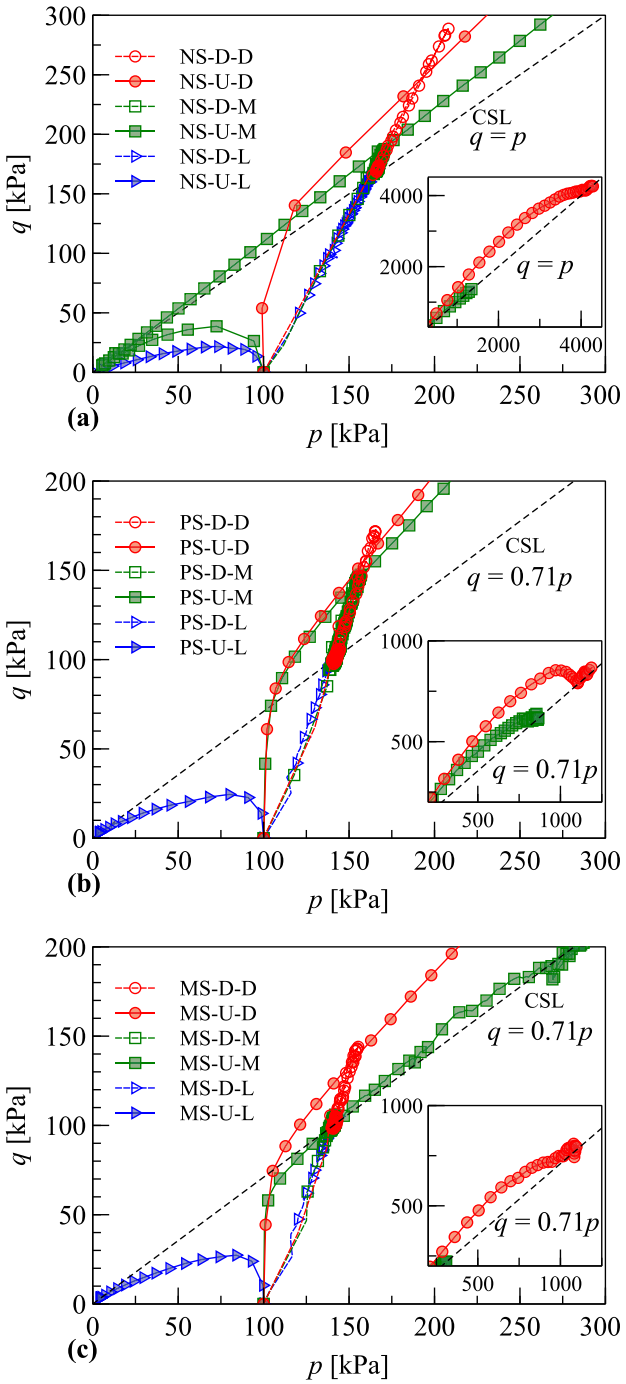

FIG. 3. Loading paths performed on the three groups of specimens. Insets are the extensions of upper-right corners of plots. CSL: critical state line.

be related to the associated changes in local internal structures (see Refs. [30,31]), which is, however, beyond the focus of this work.

We also note that all stress paths reach a unique CSL (i.e., a line denoted by a unique ratio of q/p), regardless of the initial states and loading conditions. This can be more clearly revealed from the evolution of q/p against the axial strain ϵ_z plotted in Fig. 4. The figure shows that q/p for the undrained cases is slightly larger than that for the drained cases, until they all reach an almost identical value at the

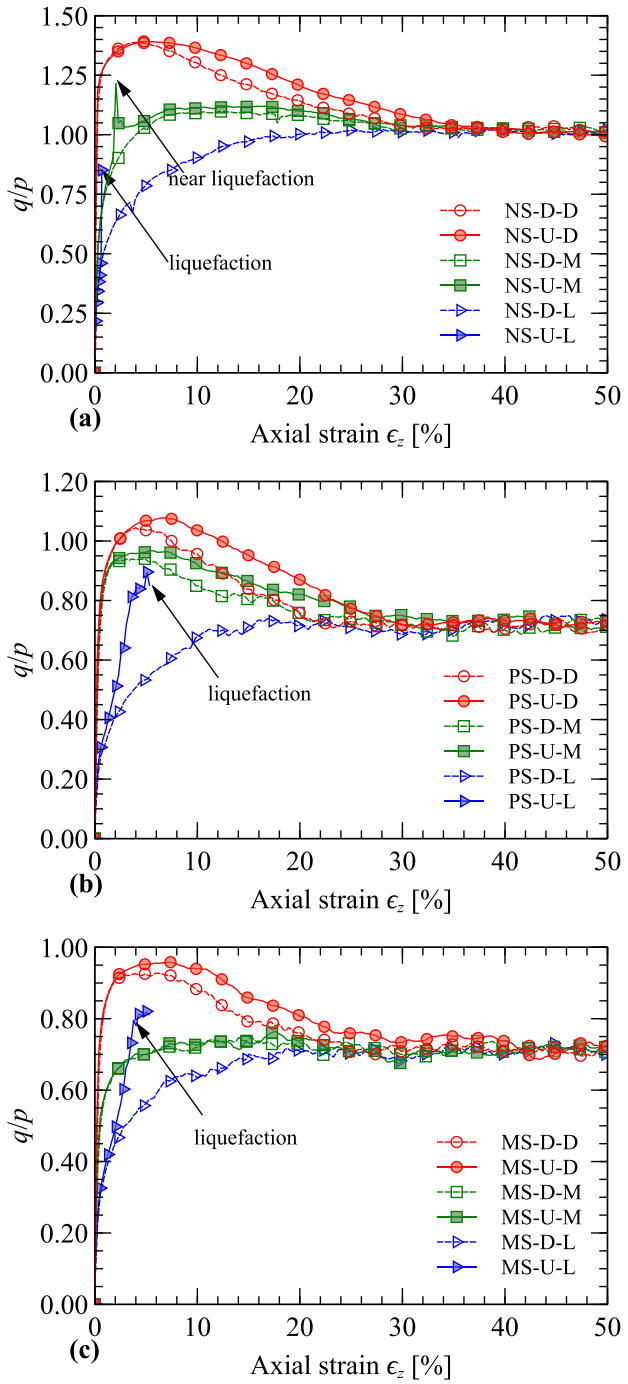

FIG. 4. Evolution of deviatoric stress ratio q/p for the three groups of specimens during shearing. Note: q/p is not available when liquefaction happens.

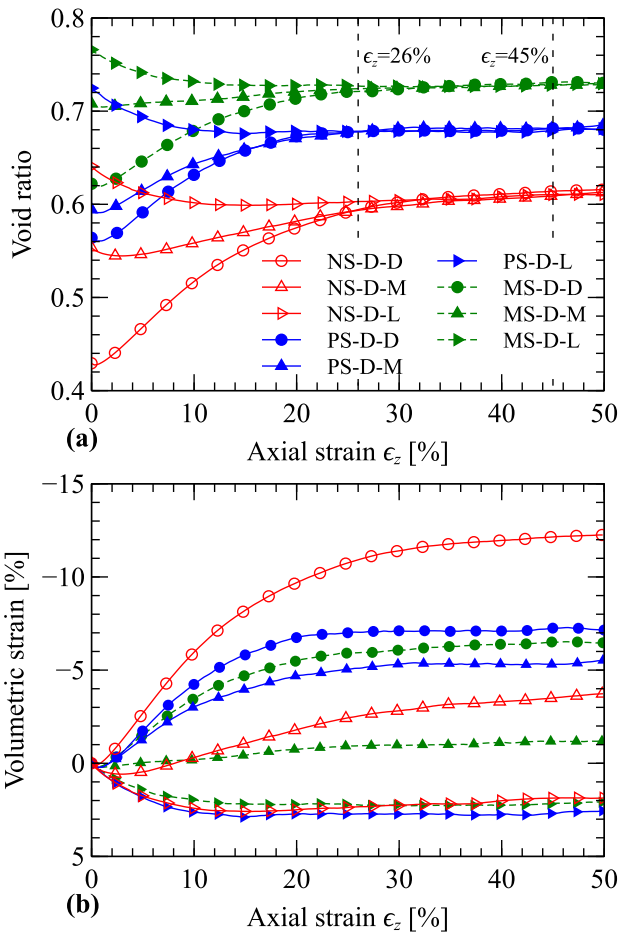

FIG. 5. Evolution of (a) void ratio and (b) volumetric strain for drained loading cases during shearing.

critical state for a given initial assembly, which is consistent with that observed in the laboratory. Moreover, it appears that the shear strength for nonsphere assemblies at the critical state is substantially enhanced due to interlocking attributable to irregular particle shapes, even though the initial assemblies may possess almost the same global solid fraction, e.g., in the cases of NS-M and PS-D (see the initial void ratio in Table II). Detailed discussion on the effects of particle shape on the stress transmission in a granular packing is beyond the scope of this work, but its significance has indeed been investigated in some early studies, e.g., Refs. [2,20–22]. Furthermore, a quick comparison of Figs. 4(b) and 4(c) reveals that the deviatoric stress ratio q/p is hardly affected by the polydispersity at the critical states (where $q/p \simeq 0.71$ for all sphere packings). Similar observations had been made by Cantor *et al.* [23] when they examined the response of polydisperse spheres subjected to simple shear.

The deformation of these specimens under drained shearing are analyzed by two macroscopic quantities, void ratio and volumetric strain, as shown in Fig. 5. As expected, all three groups of specimens reach their corresponding unique void ratios at the critical states in Fig. 5(a). It is evident that critical void ratio is a function of the constituent particles, particle shape and polydispersity being two typical factors. We show that the significance of these factors may vary in terms of their influence on shear strength and deformation. For instance, polydispersity has an insignificant effect on the critical deviatoric stress ratio but may markedly affect the critical void ratio. Furthermore, for each group of specimens in Fig. 5(b), the denser specimens experience larger volumetric strain, i.e., more significant dilation and higher peak shear strength. However, the effect of both particle shape and polydispersity on granular deformation (e.g., volumetric strain) in loose assemblies is much less apparent.

The structural and deformation characteristics of these specimens subjected to shear are further examined from a particle-scale perspective in the following sections. Three typical levels of axial strain, $\epsilon_z = 0$, 26%, and 45%, are chosen for the analyses. Note that all specimens have almost reached their corresponding steady flow regimes (or critical states) at $\epsilon_z = 26\%$.

IV. GRANULAR MICROSTRUCTURE

A. Radial distribution function

We employ the radial distribution function (RDF) $g(r)$ to examine the spatial structure of a granular packing. RDF gives the probability of finding the center of a particle at a distance of r from a reference particle. A normalized form of $g(r)$ is usually given as [32]

$$g(r) = \frac{\widetilde{\rho}(r)}{\rho} = \frac{n(r)}{4\pi r^2 \Delta r \rho}, \tag{8}$$

where $n(r)$ is the number of particles within a spherical shell occupying the space from a radial distance r to $r + \Delta r$ from the center of the reference particle; $\widetilde{\rho}(r)$ is the number density at a distance of r, equal to $n(r)/(4\pi r^2 \Delta r)$, i.e., the number of particles per unit volume within the spherical shell; and ρ is the average number density of the whole packing, i.e., the number of particles per unit volume within the packing. With such normalization, $g(r)$ tends to 1 for large r, implying that there is no long-range order. In this work, $\Delta r = 0.1\langle d \rangle$, where $\langle d \rangle$ is the mean particle diameter; $g(r)$ is averaged over all reference particles within the packing. The RDFs of the three groups of specimens at different shearing states are shown in Fig. 6, where the subscripts in the legend $_{\text{INIT}}$, $_{26}$ and $_{45}$ respectively denote the initial state and the studied states with $\epsilon_z = 26\%$ and $\epsilon_z = 45\%$.

For the specimens of monodisperse spheres in Fig. 6(c), a clear sharp peak of $g(r)$ is found to appear at a distance of one particle diameter $\langle d \rangle$, and a split peak appears in between $r = \sqrt{3}\langle d \rangle$ and $2\langle d \rangle$, which is consistent with observations reported in the literature, e.g., [11,18]. It is worth noting that $g(r)$ is theoretically zero at short distances (less than one particle diameter) for hard sphere packing due to the strong repulsive forces, but nonzero $g(r)$ is observed for $r \to \langle d \rangle$ due to a finite interval of measured radial distance (i.e., $0.1\langle d \rangle$ here). The presence of secondary local peaks following the first primary one in RDFs implies characteristic structures with rather different local patterns [6]. For example, the second local peak is dominated by spheres arranged in nearly coplanar equilateral triangles [18]. As for polydisperse spheres, i.e., PS in Fig. 6(b), the corresponding RDFs are similar to that of MS, with the first local peak appearing at a distance of one mean particle diameter. With additional distortion in particle shape, i.e., NS in Fig. 6(a), the RDFs still possess a similar shape to that for PS and MS but with apparent changes in location and amplitude of peaks. Overall, the first local peak of a RDF appears at a distance of approximately one mean particle diameter for polydisperse specimens, regardless of particle shape. It is also evident that the number of local peaks of RDFs decreases due to the effect of polydispersity and particle shape, suggesting

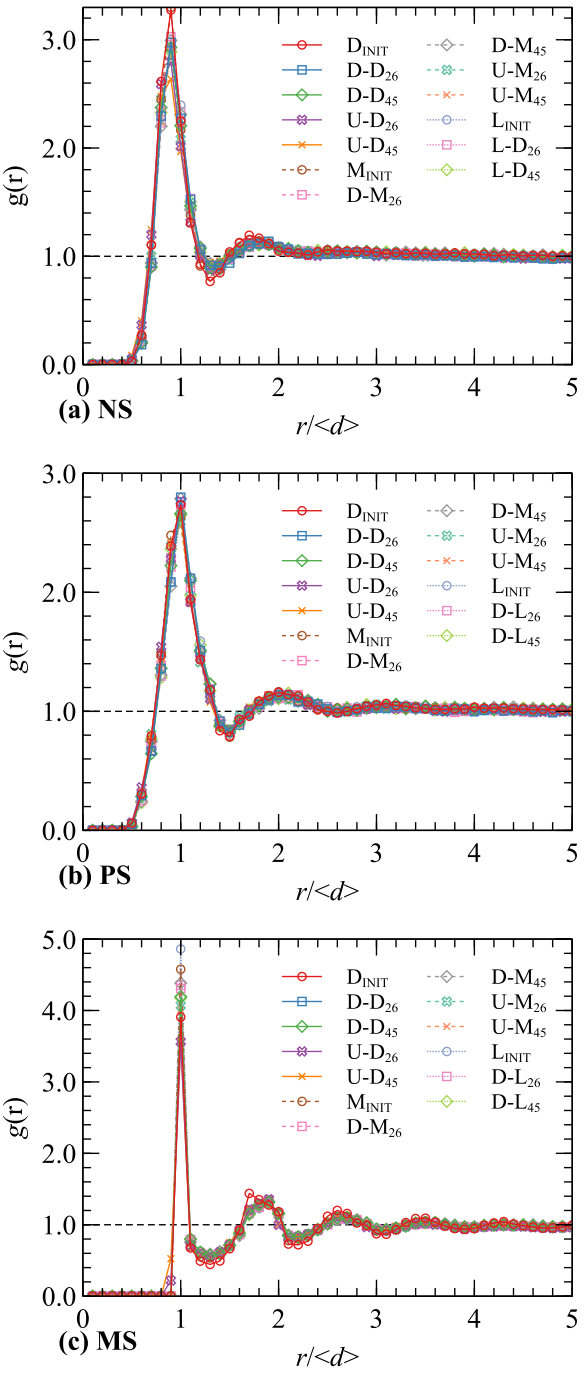

FIG. 6. Radial distribution functions (RDFs) for the three groups of specimens: (a) NS, (b) PS, (c) MS at different shearing states. The measured radial distance interval is 0.1 mean particle diameter.

that the dominant local patterns of structure within a packing are expected to be lost. However, the RDF may not be particularly suitable for disclosing local ordered structures for poly-shaped particles as it does for mono-shaped particles (e.g., Ref. [33]). Furthermore, most interestingly, for each of the three groups of specimens, despite certain small fluctuations, the RDFs remain almost unchanged during shearing and appear to be independent of initial states (dense or loose) and loading conditions (at least for the two typical loading conditions considered here). Similar observations have been

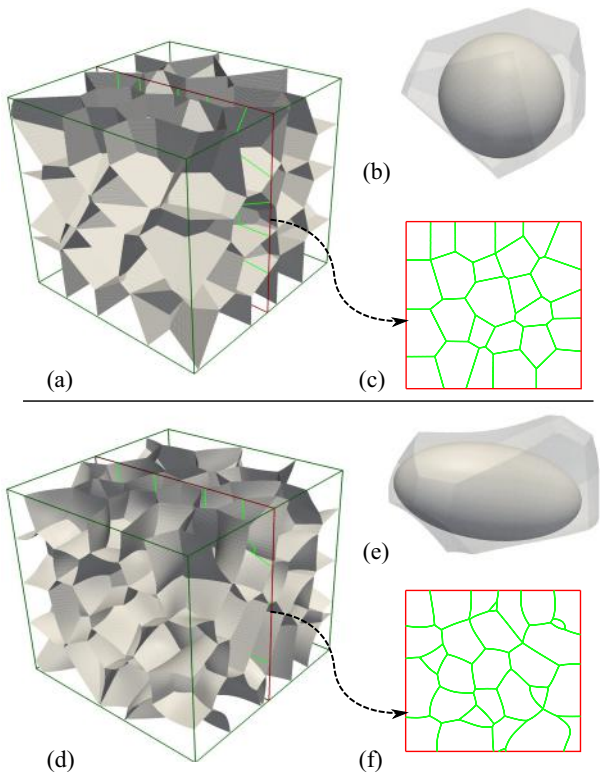

FIG. 7. Voronoi cells constructed by means of the Set Voronoi tessellation for spheres (upper) and nonspheres (lower): (a, d) networks of Voronoi cells; (b, e) a Voronoi cell enclosing a particle; (c, f) a slice of networks of Voronoi cells.

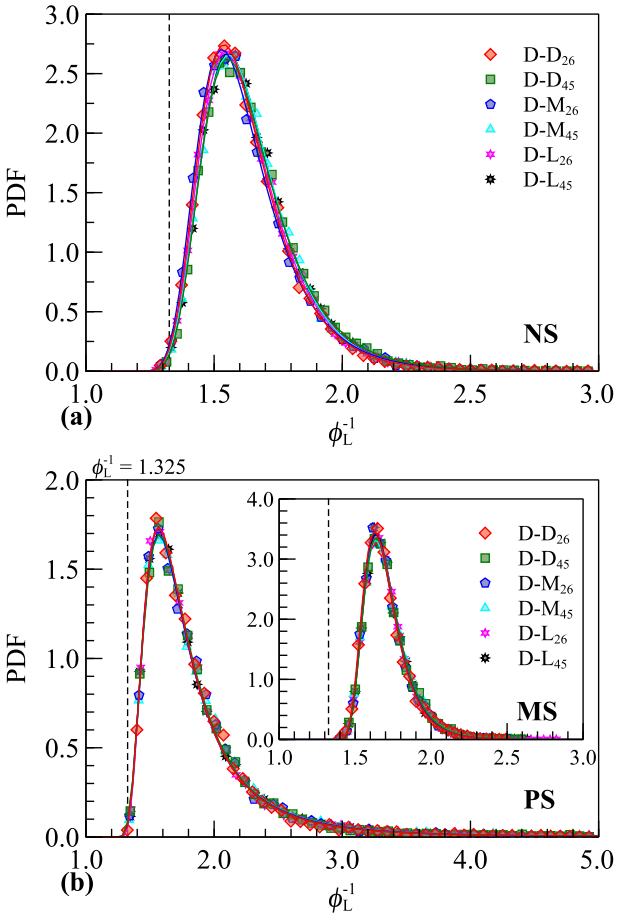

FIG. 8. Probability distribution functions (PDFs) of inverse local fraction ϕ_L^{-1} for the three groups of specimens at different drained shearing states. Lines are the best fitting with inverse Weibull distributions given in Eq. (10).

reported by Guo and Zhao [11], who simulated shear tests on sphere packings under a constant-volume shearing.

B. Local structure

1. Partition of local cells

The particle-centered method, e.g., the Voronoi tessellation, has been popular in the construction of local cells for sphere packings [6,8,11,34,35]. It is, however, nontrivial to partition local cells of nonsphere packings. Herein we employ a recently developed method named Set Voronoi tessellation to partition local cells of nonsphere packings [12,36–39]. The Set Voronoi tessellation partitions the point clouds from particle surfaces within a packing based on the general Voronoi tessellation. It yields a series of subcells partitioning the entire space of a packing where each subcell encloses one particle surface point. The subcells with particle surface points from the same particle are then merged to form the Voronoi cell enclosing the particle.

Figure 7 comparatively shows the Voronoi cells of sphere and nonsphere packings. It is clear that the shape of Voronoi cells of a nonsphere packing differs characteristically from that of a sphere packing, i.e., nonconvex shape with curved facets in Fig. 7(e) vs convex polyhedron in Fig. 7(b). Furthermore, it is worth noting that the accuracy of a Voronoi cell is dependent on the resolution of particle surface discretization, which was discussed in our previous study and others [38,40]. In this work, the surface of each particle is discretized into 600 points, yielding a relatively high resolution.

2. Inverse local fraction

The inverse local fraction ϕ_L^{-1} (i.e., the inverse of the local solid fraction within a Voronoi cell) is used to examine the fluctuation of local volume:

$$\phi_L^{-1} = \frac{V_c}{V_p}, \tag{9}$$

where V_c and V_p are volumes of a given Voronoi cell and its enclosing particle. Here emphasis is placed on the effect of loading conditions and initial states on the probability distribution of ϕ_L^{-1}. We plot the data of ϕ_L^{-1} for the three groups of specimens at drained and undrained shearing states, respectively, in Figs. 8 and 9. For the case of monodisperse samples (MS), the theoretical minimum of ϕ_L^{-1} is around 1.325 for a random packing [7], which is reproduced as the lower bound of ϕ_L^{-1} in our simulated results and is plotted in the subfigures as a reference. Moreover, it has also been reported that ϕ_L^{-1} yields a γ distribution in MS [7,11], which, however, does not hold well in the case of polydispersity. Thus, Guo and Zhao [11] proposed a mixed-γ distribution to fit the distribution of ϕ_L^{-1} in bidisperse and tridisperse sphere packings, where each monodisperse group of particles (grouped by particle radius) was fitted by a γ distribution and then weighed into

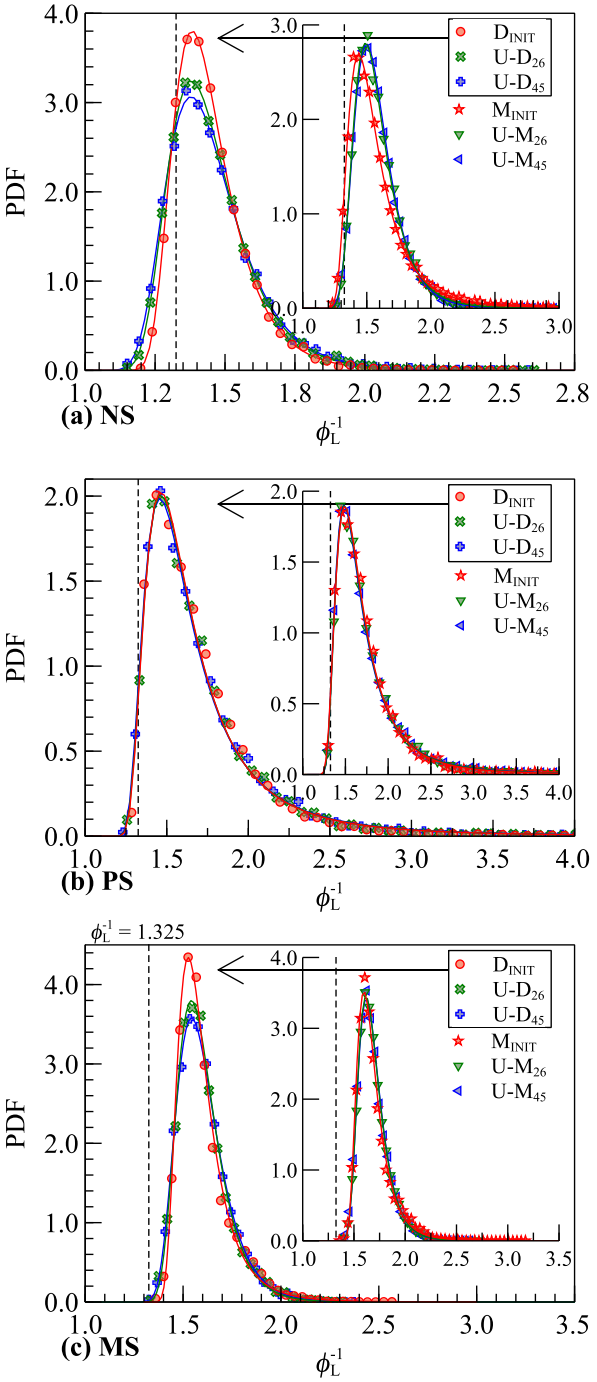

FIG. 9. Probability distribution functions (PDFs) of inverse local fraction ϕ_L^{-1} for the three groups of specimens at different undrained shearing states. Lines are the best fitting with inverse Weibull distributions given in Eq. (10).

the total distribution. Nevertheless, it is not convenient, even impossible to use the mixed-γ distribution to fit the distribution of ϕ_L^{-1} for a specimen with a continuous particle size distribution as adopted in the current study. Thus, instead of using the mixed-γ distribution, we introduce the inverse Weibull distribution to fit the distribution of ϕ_L^{-1} as follows:

$$\mathrm{PDF}\left(\phi_L^{-1}, \alpha, s, l\right) = \frac{\alpha}{s}\left(\frac{s}{\phi_L^{-1} - l}\right)^{\alpha+1} e^{-\left(\frac{s}{\phi_L^{-1}-l}\right)^{\alpha}}, \tag{10}$$

where α, s, and l are respectively shape, scale, and location parameters.

As shown in Figs. 8 and 9, the PDF of ϕ_L^{-1} can be well fitted by the inverse Weibull distribution, regardless of polydispersity in grain size or shape. We first examine the critical states ($\epsilon_z = 26\%$ and 45%) of the drained case in Fig. 8 where the global solid fraction remains almost constant for each group of specimens. It is clear that the distributions of ϕ_L^{-1} for each group roughly collapse into a single PDF. This feature also holds for the critical states of the undrained case in Fig. 9. Therefore, it can be concluded that the inverse local fraction follows a unique distribution for assemblies with the same constituent particles at the critical states (or steady flow regimes). An (approximately) identical global solid fraction may serve as a necessary condition for the unique PDF of ϕ_L^{-1}. Indeed, previous studies on packings of monodisperse ellipsoids reported that ϕ_L^{-1} has an almost persistent distribution independent of particle shape for a given global solid fraction [36,38]. However, in the presence of both polydispersities in particle size and shape, the PDF of ϕ_L^{-1} is no longer unique for a given global solid fraction, which can be readily verified by comparing D-L_{26} for NS in Fig. 8(a) and U-M_{26} for PS in Fig. 9(b). The shearing plays an extra important role. For example, referring to Fig. 9, for each group of specimens, the global solid fraction is identical due to the constant-volume condition, but one finds that the PDF of ϕ_L^{-1} at the initial state evidently differs from that at the critical states for dense specimens.

Based on normalization of the inverse local fraction according to

$$\hat{\phi}_L = \frac{\phi_L^{-1} - \phi_{L\min}^{-1}}{\langle \phi_L^{-1} \rangle - \phi_{L\min}^{-1}}, \tag{11}$$

where $\langle \phi_L^{-1} \rangle$ and $\phi_{L\min}^{-1}$ are the mean and minimum of ϕ_L^{-1}, and it has been found that $\hat{\phi}_L$ follows a k-γ distribution, independent of the global solid fraction for MS [7,8,11]. Figure 10 shows that the normalized inverse local fraction collapses to a single probability distribution not only for packings with monodisperse spheres but also for packings with polydisperse spheres or nonspheres. Moreover, this universality still holds for different loading conditions. Furthermore, this unique probability distribution of $\hat{\phi}_L$, which holds regardless of initial states and loading conditions, can be well fitted by the following log-normal distribution:

$$\mathrm{PDF}(x, \sigma, \mu) = \frac{1}{x\sigma\sqrt{2\pi}} e^{-\frac{[\ln(x)-\mu]^2}{2\sigma^2}}, \tag{12}$$

where σ and μ are respectively scale and location parameters for the normally distributed logarithm $\ln(x)$.

3. Anisotropy of local cells

The Minkowski functionals and Minkowski tensors have been widely applied to analyzing the morphology of complex spatial microstructures [41,42]. In this study, we employ the following Minkowski functional W_1 and the Minkowski tensor $\mathbf{W}_1^{0,2}$ to quantify the morphology of each individual

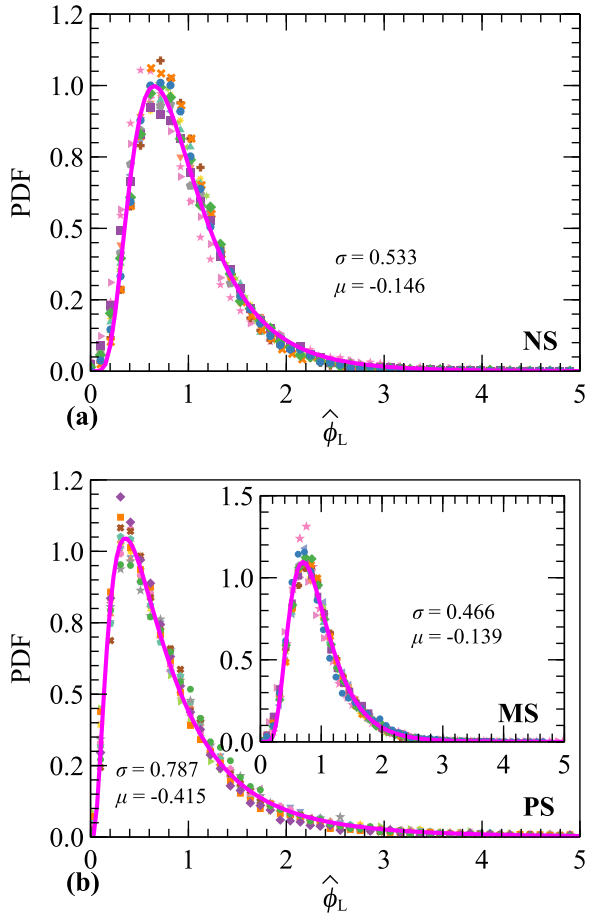

FIG. 10. Probability distribution functions (PDFs) of normalized inverse local fraction $\hat{\phi}_L$ for the three groups. The collapsed symbols include all data at the three shearing levels ($\epsilon_z = 0, 26\%$ and 45%) for all initial states and loading conditions. Lines are the best fitting with log-normal distributions given in Eq. (12).

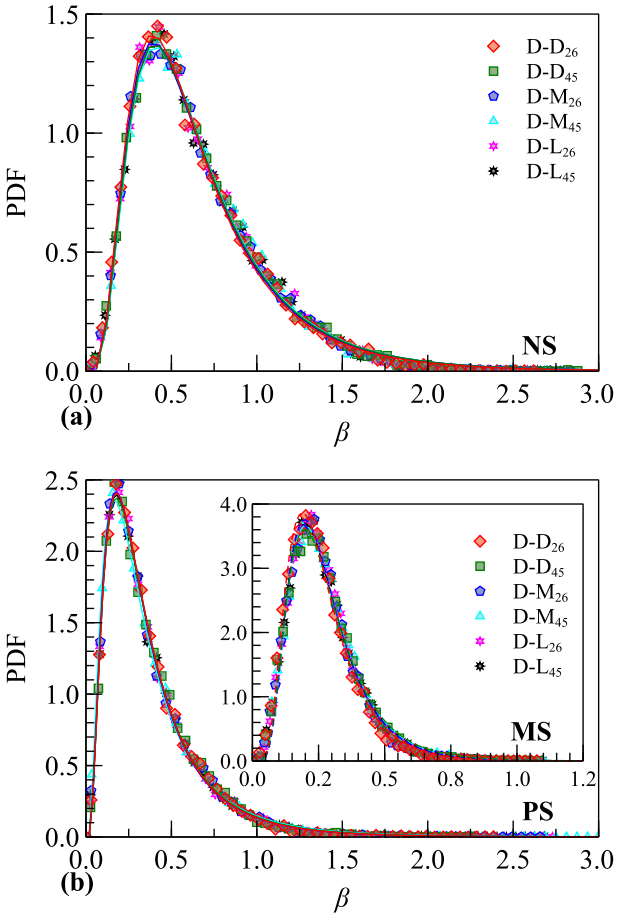

FIG. 11. Probability distribution functions (PDFs) of local anisotropy β for the three groups of specimens at different drained shearing states. Lines are the best fitting with log-normal distributions given in Eq. (12).

local cell:

$$W_1 = \frac{1}{3}\int_\Lambda dA, \tag{13}$$

$$\mathbf{W}_1^{0,2} = \frac{1}{3}\int_\Lambda \mathbf{n}\otimes\mathbf{n}dA, \tag{14}$$

where Λ is the cell surface, dA is the scalar infinitesimal area element, and $\mathbf{n}$ is the outward normal vector of the cell surface. Using W_1 to normalize $\mathbf{W}_1^{0,2}$ yields a dimensionless tensor $\mathbf{\Phi}$ with a unity trace:

$$\mathbf{\Phi} = \frac{\mathbf{W}_1^{0,2}}{W_1}, \tag{15}$$

so that the cell is defined to be isotropic if and only if the three eigenvalues of $\mathbf{\Phi}$ ($|\lambda_1| \leqslant |\lambda_2| \leqslant |\lambda_3|$) are equal. Anisotropy of a local cell is characterized by the deviation from isotropy. We introduce the following anisotropy index β according to [11,42]

$$\beta = \left|\frac{\lambda_3}{\lambda_1}\right| - 1, \tag{16}$$

where $\beta \geqslant 0$; $\beta = 0$ corresponds to an isotropic cell, and a larger value of β suggests the cell is more anisotropic.

The probability distribution functions (PDFs) of β at different shearing states for drained and undrained shear are respectively shown in Figs. 11 and 12. Notably, all PDFs of β can be well fitted according to the log-normal distribution given in Eq. (12), which appears to hold universally for all loading conditions. Unsurprisingly, the case of PS shows wider distributions of β than MS due to significantly increased irregularity in cell shape caused from polydispersity in particle size, referring to Fig. 11(b) or Figs. 12(b) and 12(c). In addition to size polydispersity, nonspherical particles in Figs. 11(a) and 12(a) are expected to render the cell shape more irregular (see Fig. 7), thereby leading to wider distributions of β, i.e., stronger anisotropy in cell shape. Moreover, notably, at the critical (steady) states for both drained and undrained shear, the PDFs of β collapse into a single PDF, similar to the distribution of ϕ_L^{-1} in the last section. As for the initial state, whether its PDF of β collapses into the PDFs at the critical states dominantly depends on how far the initial state is from the critical states. A medium-dense initial state is much closer to the critical state, so that the PDFs of β collapse

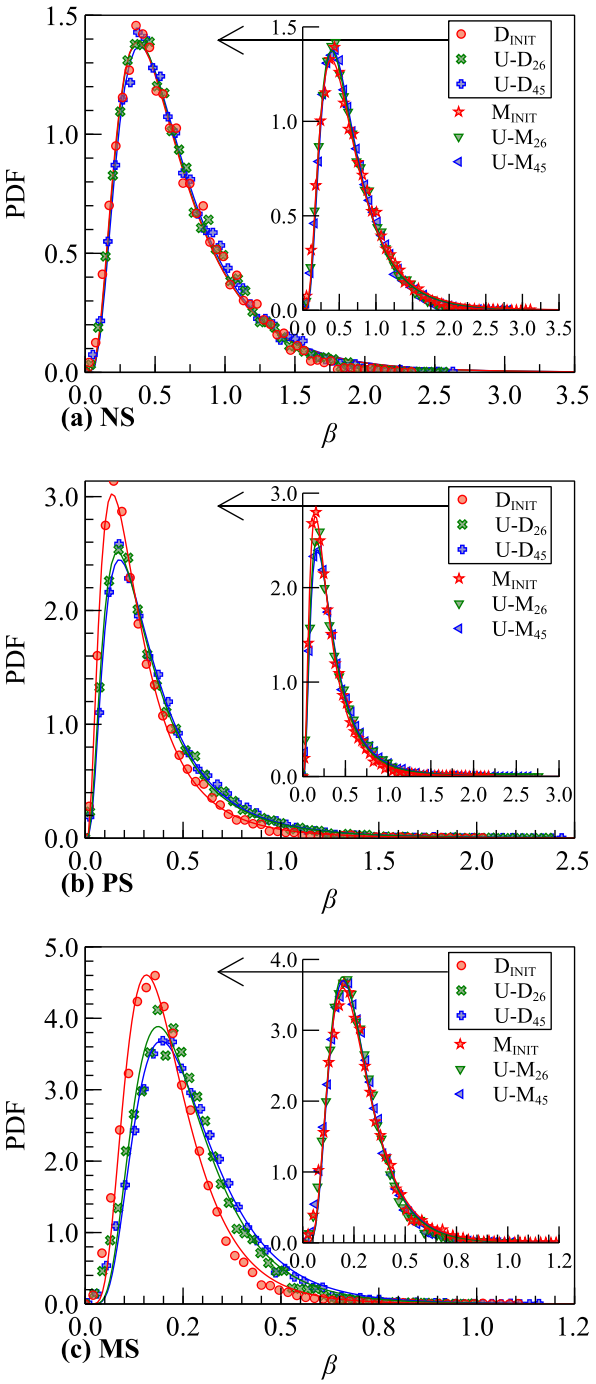

FIG. 12. Probability distribution functions (PDFs) of local anisotropy β for the three groups of specimens at different undrained shearing states. Lines are the best fitting with log-normal distributions given in Eq. (12).

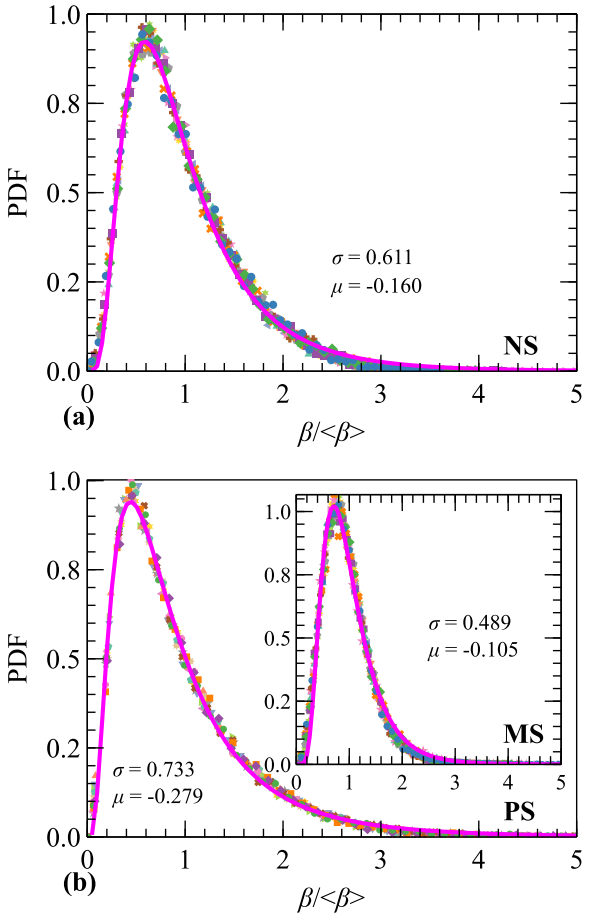

FIG. 13. Probability distribution functions (PDFs) of normalized local anisotropy $\beta/\langle\beta\rangle$ for the three groups. The collapsed symbols include all data at the three shearing levels ($\epsilon_z = 0$, 26% and 45%) for all initial states and loading conditions. Lines are the best fitting with log-normal distributions given in Eq. (12).

into a single one for both sheared and unsheared states (see the insets in Fig. 12).

To sum up, the distribution of anisotropy index β is found to remain almost unchanged during steady shearing for both spherical and nonspherical packings, which is independent of the initial states and loading conditions. For sheared packings with specified constituent particles, the corresponding PDFs of β are strongly determined by the global solid fraction. Based on a normalization of β with its corresponding average $\langle\beta\rangle$ [11], all PDFs of $\beta/\langle\beta\rangle$ consistently collapse into a single curve which can be fitted by a log-normal distribution, as is shown in Fig. 13. This universality holds for both spherical and nonspherical packings and is not affected by the initial states and loading conditions.

C. Local deformation

The Voronoi cells partitioning the entire space of a packing undergo nonuniform deformation during shearing. Assuming the subspace occupied by each local Voronoi cell is deformed uniformly, we introduce the following two quantities ϵ_{vL} and ϵ_{sL} to characterize the local deformation

$$\epsilon_{vL} = \ln\left(\frac{V_c}{V_{c0}}\right), \quad \epsilon_{sL} = \ln\left(\frac{S_c}{S_{c0}}\right), \tag{17}$$

where V_c and V_{c0} are cell volumes at the sheared and unsheared (initial) states, respectively, and S_c and S_{c0} are anisotropy of cell shape at the sheared and unsheared (initial) states, respectively, with $S_c = (\lambda_1 - \lambda_2)^2 + (\lambda_1 - \lambda_3)^2 + (\lambda_2 - \lambda_3)^2$, where $\lambda_i (i = 1, 2, 3)$ are the three eigenvalues of $\mathbf{\Phi}$ in Eq. (15).

With the above definition, ϵ_{vL} can be regarded as a local volumetric strain quantifying the degree of volumetric change for a given cell during shearing, while ϵ_{sL} measures the distortion in cell shape excluding the change in volume so that it is reasonable to use ϵ_{sL} to partially represent the shear strain experienced by the cell. We note that it is nontrivial to define local shear strain in terms of the distortion of cell shape due to its extreme irregularity. There are indeed alternative approaches for defining local strain within a granular material, e.g., Bagi's strain [43] based on tetrahedral cells constructed by tessellating particle centers. The Bagi method, however, by which the tetrahedral cell definitely intersects with its associated particles, is not applicable to our case for a Voronoi cell enclosing a single particle. ϵ_{sL} can be called a local pseudoshear strain.

For the local volumetric strain, it is normalized as $\hat{\epsilon}_{vL} = (\epsilon_{vL} - \epsilon_{vg})/\sigma_{\epsilon_{vL}}$, where ϵ_{vg} is the global volumetric strain (see Fig. 5) that is equal to the volume-averaged ϵ_{vL} over all cells and $\sigma_{\epsilon_{vL}}$ is the standard deviation of ϵ_{vL}. The distributions of $\hat{\epsilon}_{vL}$ for all sheared states are plotted in Fig. 14, which can be well fitted by using the Gaussian distribution. Specifically, in the cases of MS, all data of $\hat{\epsilon}_{vL}$ collapse to a single distribution (resembling a standard normal distribution); however, in the presence of polydispersity in PS cases, fluctuations occur at peaks of the distributions of $\hat{\epsilon}_{vL}$. In the cases of NS, it is of interest to observe that all data of $\hat{\epsilon}_{vL}$ collapse to three different distributions corresponding to the three different initial states, respectively, suggesting that the local deformation of nonsphere packings is dependent more on the initial states than in the case of sphere packings. Similar universality is also found in the distribution of local pseudoshear strain. As shown in Fig. 15, the shifted local pseudoshear strain $\hat{\epsilon}_{sL}$ $(= \epsilon_{sL} - \langle\epsilon_{sL}\rangle$, where $\langle\epsilon_{sL}\rangle$ is the mean of $\epsilon_{sL})$ follows almost identical Gaussian distributions for each group of specimens, despite certain fluctuations in peaks for NS. Compared with sphere packings in PS and MS, nonsphere packings in NS exhibit narrower distributions in $\hat{\epsilon}_{sL}$, implying that stronger localization takes place within nonsphere packings.

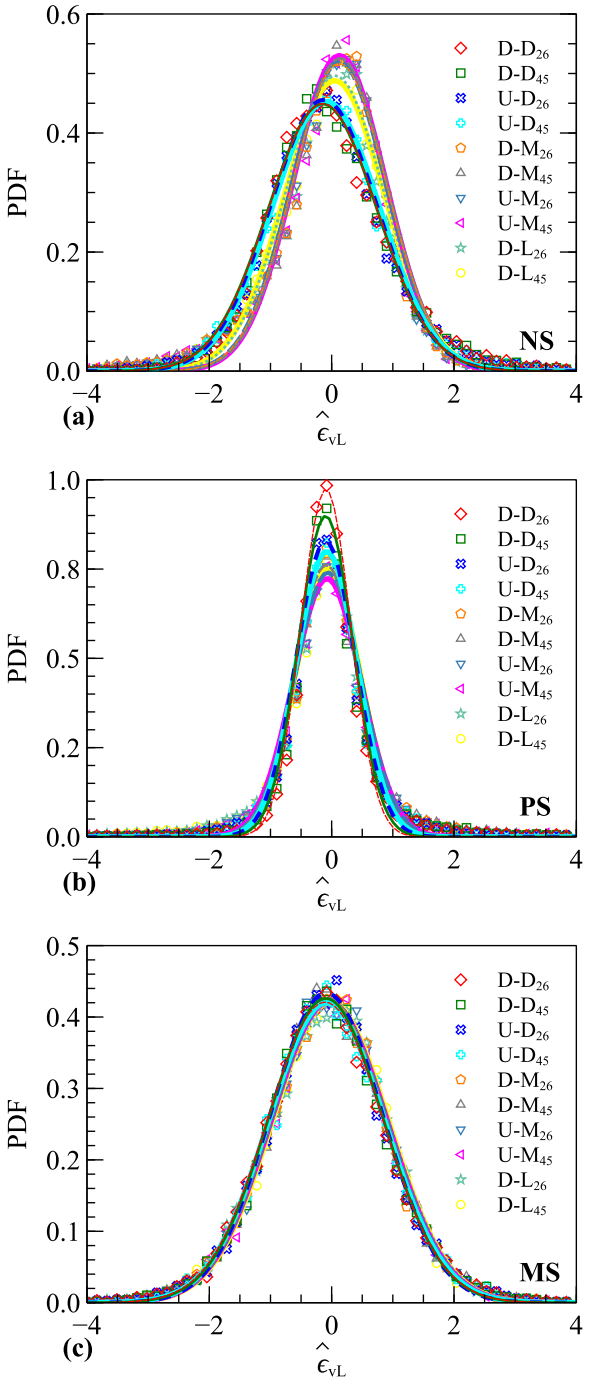

FIG. 14. Probability distribution functions (PDFs) of normalized local volumetric strain $\hat{\epsilon}_{vL}$ for the three groups. Lines are the best fitting with Gaussian distributions.

V. SUMMARY

A comprehensive comparison was presented for the shear response of granular materials composed of spherical and nonspherical particles with different polydispersities (mono- and ploy-dispersed), initial states (dense, medium dense, and loose), and loading conditions (drained and undrained) based on 3D discrete element simulations. The following conclusive observations are reached:

(1) As a measure of local structure, the radial distribution function (RDF) shows similar shapes for granular materials regardless of their polydispersity in both particle size and shape. The first primal peak of RDF is found to appear at a distance of one mean particle diameter. For a specimen with given constituent particles (i.e., constant polydispersity in both particle size and shape), all RDFs collapse into a single curve independent of initial states and loading conditions, despite certain small fluctuations during shearing. The number of local peaks in a RDF decreases with increased polydispersity in particle size and shape, suggesting that the dominant local patterns of structure within a packing are weakened and the entire local structure becomes more homogenized. In this case, the RDF may lose its strength to disclose more details of the spatial structure.

(2) The Set Voronoi tessellation [40] has been used to analyze the local structure and deformation of sphere and nonsphere packings. At the particle scale, both the inverse local fraction ϕ_L^{-1} and anisotropy index β are found to respectively follow the inverse Weibull and the log-normal distributions, and both distributions become unique at the critical state,

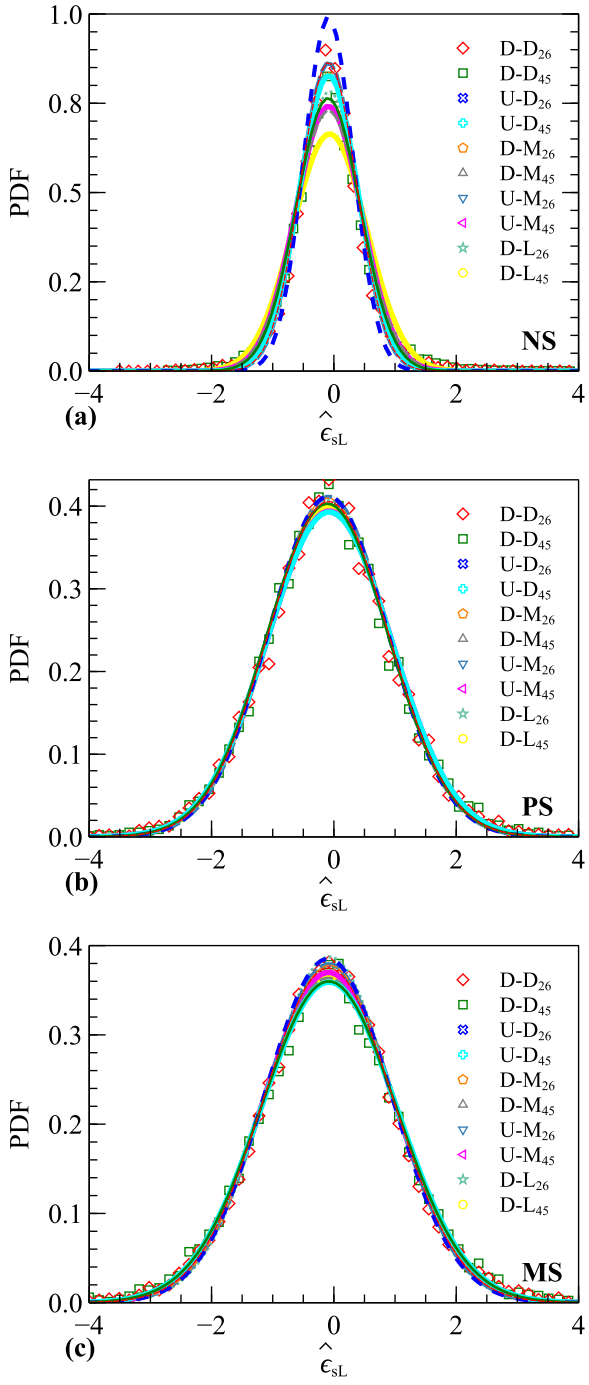

FIG. 15. Probability distribution functions (PDFs) of shifted local pseudoshear strain $\hat{\epsilon}_{sL}$ for the three groups. Lines are the best fitting with Gaussian distributions.

totally erasing their memory of initial states and loading conditions (or paths). With certain normalization of ϕ_L^{-1} and β, their corresponding distributions further collapse into a single curve for all states during shearing, which can be well fitted by using the log-normal distribution. This universality holds not only for monodisperse sphere packings as reported in previous studies [7,11] but also for packings of polydisperse poly-shaped nonspheres, regardless of initial states and loading conditions. In other words, the distribution is only affected by the polydispersity in both particle size and shape.

(3) The local deformations during shear, measured by the local volumetric strain ϵ_{vL} and local pseudoshear strain ϵ_{sL}, are found to follow Gaussian distributions. For both monodisperse and polydisperse spherical packings, the normalized ϵ_{vL} and ϵ_{sL} follow almost identical Gaussian distributions which are independent of the initial states and loading conditions. However, for polydisperse nonsphere packings, the collapsed Gaussian distribution of the normalized ϵ_{vL} is dependent on the initial states, while the normalized ϵ_{sL} collapses to a single distribution with certain fluctuations at peaks. The above comparison between spherical and nonspherical packings suggests that the universality in sphere packings might not hold for nonsphere packings, highlighting the importance of considering the role played by particle shape in the shear response of granular materials.

This paper constitutes a first step towards exploring the role of grain shape in the universal internal structure properties of granular materials under shear. In line with this, there are several aspects worthy of future research: (1) the validation of the presented conclusions for extremely distorted particle shapes, e.g., needlelike particles with a significant large aspect ratio, and for nonconvex particles (e.g., by clumping convex shapes); and (2) possible provision of rigorous analytical derivations and explanations on the observed universal distribution based on statistical mechanics.

ACKNOWLEDGMENTS

This work was financially supported by the Hong Kong Scholars Program (2018), the National Natural Science Foundation of China (by Projects No. 51679207, No. 51809229, No. 51909095, and No. 11972030), and the Research Grants Council of Hong Kong (by GRF Project No. 16205418, TBRS Project No. T22-603/15N, and CRF Project No. C6012-15G). Any opinions, findings, and conclusions or recommendations expressed in this material are those of the authors and do not necessarily reflect the views of the financial bodies.

[1] F. Radjai, D. E. Wolf, M. Jean, and J.-J. Moreau, Bimodal Character of Stress Transmission in Granular Packings, Phys. Rev. Lett. **80**, 61 (1998).

[2] E. Azéma, F. Radjai, B. Saint-Cyr, J.-Y. Delenne, and P. Sornay, Rheology of three-dimensional packings of aggregates: Microstructure and effects of nonconvexity, Phys. Rev. E **87**, 052205 (2013).

[3] J. Fonseca, C. O'Sullivan, M. Coop, and P. Lee, Quantifying the evolution of soil fabric during shearing using scalar parameters, Géotechnique **63**, 818 (2013).

[4] S. F. Edwards and R. Oakeshott, Theory of powders, Physica A **157**, 1080 (1989).

[5] A. Mehta and S. Edwards, Statistical mechanics of powder mixtures, Physica A **157**, 1091 (1989).

[6] T. Aste, Variations around disordered close packing, J. Phys.: Condens. Matter **17**, S2361 (2005).

[7] T. Aste, T. Di Matteo, M. Saadatfar, T. J. Senden, M. Schröter, and H. L. Swinney, An invariant distribution in static granular media, Europhys. Lett. **79**, 24003 (2007).

[8] T. Aste and T. Di Matteo, Emergence of gamma distributions in granular materials and packing models, Phys. Rev. E **77**, 021309 (2008).

[9] J. G. Puckett and K. E. Daniels, Equilibrating Temperaturelike Variables in Jammed Granular Subsystems, Phys. Rev. Lett. **110**, 058001 (2013).

[10] S.-C. Zhao and M. Schröter, Measuring the configurational temperature of a binary disk packing, Soft Matter **10**, 4208 (2014).

[11] N. Guo and J. Zhao, Local fluctuations and spatial correlations in granular flows under constant-volume quasistatic shear, Phys. Rev. E **89**, 042208 (2014).

[12] F. M. Schaller, S. C. Kapfer, J. E. Hilton, P. W. Cleary, K. Mecke, C. De Michele, T. Schilling, M. Saadatfar, M. Schröter, G. W. Delaney *et al.*, Non-universal Voronoi cell shapes in amorphous ellipsoid packs, Europhys. Lett. **111**, 24002 (2015).

[13] K. Wang, C. Song, P. Wang, and H. A. Makse, Edwards thermodynamics of the jamming transition for frictionless packings: Ergodicity test and role of angoricity and compactivity, Phys. Rev. E **86**, 011305 (2012).

[14] V. Chikkadi and P. Schall, Nonaffine measures of particle displacements in sheared colloidal glasses, Phys. Rev. E **85**, 031402 (2012).

[15] G. MiDi, On dense granular flows, Eur. Phys. J. E **14**, 341 (2004).

[16] P. Jop, Y. Forterre, and O. Pouliquen, A constitutive law for dense granular flows, Nature (London) **441**, 727 (2006).

[17] J. Zhao and N. Guo, Unique critical state characteristics in granular media considering fabric anisotropy, Géotechnique **63**, 695 (2013).

[18] P. Parafiniuk, M. Molenda, and J. Horabik, Influence of particle shape and sample width on uniaxial compression of assembly of prolate spheroids examined by discrete element method, Physica A **416**, 279 (2014).

[19] S. Zhao, T. Evans, and X. Zhou, Effects of curvature-related DEM contact model on the macro-and micro-mechanical behaviours of granular soils, Géotechnique **68**, 1085 (2018).

[20] E. Azéma, F. Radjai, and G. Saussine, Quasistatic rheology, force transmission and fabric properties of a packing of irregular polyhedral particles, Mech. Mater. **41**, 729 (2009).

[21] E. Azéma and F. Radjai, Force chains and contact network topology in sheared packings of elongated particles, Phys. Rev. E **85**, 031303 (2012).

[22] S. Zhao and X. Zhou, Effects of particle asphericity on the macro-and micro-mechanical behaviors of granular assemblies, Granular Matter **19**, 38 (2017).

[23] D. Cantor, E. Azéma, P. Sornay, and F. Radjai, Rheology and structure of polydisperse three-dimensional packings of spheres, Phys. Rev. E **98**, 052910 (2018).

[24] S. Zhao and J. Zhao, A poly-superellipsoid-based approach on particle morphology for DEM modeling of granular media, Int. J. Numer. Anal. Methods Geomech. **43**, 2147 (2019).

[25] S. Zhao, N. Zhang, X. Zhou, and L. Zhang, Particle shape effects on fabric of granular random packing, Powder Technol. **310**, 175 (2017).

[26] G. W. Delaney and P. W. Cleary, The packing properties of superellipsoids, Europhys. Lett. **89**, 34002 (2010).

[27] X. S. Shi, J. Nie, J. Zhao, and Y. Gao, A homogenization equation for the small strain stiffness of gap-graded granular materials, Comput. Geotech. (2020) doi:10.1016/j.compgeo.2020.103440.

[28] N. Guo and J. Zhao, The signature of shear-induced anisotropy in granular media, Comput. Geotech. **47**, 1 (2013).

[29] J. Christoffersen, M. Mehrabadi, and S. Nemat-Nasser, A micromechanical description of granular material behavior, J. Appl. Mech. **48**, 339 (1981).

[30] J. Wei, D. Huang, and G. Wang, Microscale descriptors for particle-void distribution and jamming transition in pre- and post-liquefaction of granular soils, J. Eng. Mech. **144**, 04018067 (2018).

[31] L. Zhang and T. M. Evans, Boundary effects in discrete element method modeling of undrained cyclic triaxial and simple shear element tests, Granular Matter **20**, 60 (2018).

[32] J. Wiącek, Geometrical parameters of binary granular mixtures with size ratio and volume fraction: Experiments and DEM simulations, Granular Matter **18**, 42 (2016).

[33] J. Zhao, S. Li, R. Zou, and A. Yu, Dense random packings of spherocylinders, Soft Matter **8**, 1003 (2012).

[34] L. Y. Yi, K. J. Dong, R. P. Zou, and A. B. Yu, Radical tessellation of the packing of spheres with a log-normal size distribution, Phys. Rev. E **92**, 032201 (2015).

[35] S. Zhao, T. M. Evans, X. Zhou, and S. Zhou, Discrete element method investigation on thermally-induced shakedown of granular materials, Granular Matter **19**, 11 (2017).

[36] F. M. Schaller, M. Neudecker, M. Saadatfar, G. W. Delaney, G. E. Schröder-Turk, and M. Schröter, Local Origin of Global Contact Numbers in Frictional Ellipsoid Packings, Phys. Rev. Lett. **114**, 158001 (2015).

[37] F. M. Schaller, R. F. B. Weigel, and S. C. Kapfer, Densest Local Structures of Uniaxial Ellipsoids, Phys. Rev. X **6**, 041032 (2016).

[38] S. Zhao, T. M. Evans, and X. Zhou, Three-dimensional Voronoi analysis of monodisperse ellipsoids during triaxial shear, Powder Technol. **323**, 323 (2018).

[39] L. Liu, Z. Yu, W. Jin, Y. Yuan, and S. Li, Uniform and decoupled shape effects on the maximally dense random packings of hard superellipsoids, Powder Technol. **338**, 67 (2018).

[40] F. M. Schaller, S. C. Kapfer, M. E. Evans, M. J. Hoffmann, T. Aste, M. Saadatfar, K. Mecke, G. W. Delaney, and G. E. Schröder-Turk, Set Voronoi diagrams of 3D assemblies of aspherical particles, Philos. Mag. **93**, 3993 (2013).

[41] G. E. Schröder-Turk, W. Mickel, S. C. Kapfer, M. A. Klatt, F. M. Schaller, M. J. Hoffmann, N. Kleppmann, P. Armstrong, A. Inayat, D. Hug *et al.*, Minkowski tensor shape analysis of cellular, granular and porous structures, Adv. Mater. **23**, 2535 (2011).

[42] G. E. Schröder-Turk, W. Mickel, S. C. Kapfer, F. M. Schaller, B. Breidenbach, D. Hug, and K. Mecke, Minkowski tensors of anisotropic spatial structure, New J. Phys. **15**, 083028 (2013).

[43] K. Bagi, Analysis of microstructural strain tensors for granular assemblies, Int. J. Solids Struct. **43**, 3166 (2006).